AIAA JOURNAL
Vol. 36, No. 4, April 1998

Prediction of the Three-Dimensional Turbulent Boundary Layer over a Swept Bump

Xiaohua Wu* and Kyle D. Squires†
Arizona State University, Tempe, Arizona 85287-6106

Large eddy simulation (LES) and Reynolds-averaged Navier–Stokes (RANS) computations have been used for prediction of a spatially developing three-dimensional turbulent boundary layer over a bump swept at 45 deg with respect to the upstream flow. Subgrid-scale stresses in the LES were parameterized using the dynamic eddy viscosity model. Reynolds stresses in the RANS calculations were closed using the v^2–f model and Spalart–Allmaras one-equation model. In the calculations, a zero-pressure gradient, statistically two-dimensional boundary layer at momentum thickness Reynolds number 3.8×10^3 is introduced one-half chord length upstream of the onset of curvature. The flow is statistically homogeneous along the coordinate parallel to the bump axis and is subject to combined perturbations in streamwise pressure gradient, spanwise pressure gradient, and surface curvature. The turning angle of the wall shear stress measured with respect to the upstream flow changes sign twice due to the alternating spanwise pressure gradient, with a maximum of more than 45 deg near the trailing edge. No-slip conditions were imposed on solid boundaries in RANS, whereas algebraic approximate boundary conditions were applied in the LES to model the near-wall flow. Mean wall shear stresses, necessary to close the approximate boundary conditions, were supplied from either experimental measurements or a separate RANS calculation. In general, the agreement between simulation and experiment in the present work is comparable to that previously obtained for the two-dimensional boundary layer at zero sweep angle. The mean flow is accurately predicted using both techniques, with some discrepancy occurring in prediction of the mean crossflow in the LES. Second-order statistics in the LES are in good agreement with measurements; RANS predictions of turbulence kinetic energy are slightly less accurate.

I. Introduction

SPATIALLY developing three-dimensional turbulent boundary layers (TBLs) are important to a variety of applications, e.g., the boundary layer over a swept wing, around a submerged vehicle, and the flow over turbine or compressor blades. In applications, three-dimensional TBLs are often generated due to a streamwise variation in geometry. A spanwise pressure gradient develops that skews the flow, with the crossflow velocity increasing from zero at the boundary-layer edge to a maximum and then back to zero at the wall to satisfy the no-slip condition. The turning of the velocity vector is measured by the angle between the wall shear stress and direction of the freestream flow. In some spatially developing three-dimensional TBLs, this angle will reverse sign with downstream evolution, e.g., Refs. 1 and 2. In addition, other complicating features of three-dimensional TBLs that have been measured in experiments show that in the outer layer the vector formed by the turbulent stress parallel to the wall is not aligned with the mean strain rate and there is a reduction in the stress-intensity ratio as compared to two-dimensional boundary layers, e.g., Refs. 3–7.

In addition to experiments, direct numerical simulation (DNS) has been used to study three-dimensional TBLs. Whereas the well-known restriction to canonical flows at low Reynolds numbers makes it difficult to apply to spatially developing three-dimensional TBLs, DNS has been a useful tool for exploring the underlying physics of these flows. Moin et al.,[8] Senstad and Moin,[9] Coleman et al.,[10,11] and Piomelli et al.[12] applied spanwise shearing forces or transverse strains to fully developed turbulent channel flow. Consistent with experiments, the simulations show a reduction in the Reynolds shear stress as well as in the turbulence kinetic energy with increasing transverse strains. The directions of the Reynolds shear stress vector and the mean velocity gradient vector were also different, with the stress lagging the mean strain as noted in experiments. Coleman et al.[11] found that the flow was more sensitive to the strains resulting from a streamwise pressure gradient than those associated with mean-flow skewing.

These and other features challenge turbulence models, and accurate prediction of three-dimensional TBLs remains difficult and continues to be one of the primary pacing items for application of computational fluid dynamics to complex flows. As discussed in Refs. 1 and 13, one problem associated with assessing predictive techniques for three-dimensional TBLs is a relative lack of comprehensive comparisons between simulation and experiment. The specific aim of this study is to apply two techniques, large eddy simulation (LES) and Reynolds-averaged Navier–Stokes (RANS), for prediction of complex spatially developing three-dimensional TBLs and assess their accuracy through comparison to experimental measurements.

In LES only the smallest, unresolved scales of motion are modeled. The large, energy-containing eddies are computed directly. This should be an advantage in simulation of complex flows such as three-dimensional TBLs because, although the large eddies may be altered by mean-flow three dimensionality, streamwise pressure gradient, and other effects resulting from variations in geometry such as curvature, the small eddies probably respond more rapidly to perturbations. Therefore, it is still reasonable to model the small scales using simple closures, especially closures sensitive to local properties of the flow such as dynamic models. In dynamic modeling, the subgrid-scale (SGS) eddy viscosity is calculated using the resolved field rather than being provided as input in advance. This feature allows the model to respond naturally to changes in the turbulence caused by external perturbations. LES and dynamic SGS models have been successfully applied to prediction of a variety of flows, e.g., Refs. 14–23. Whereas the focus of the majority of these studies has been on statistically two-dimensional flows, recent applications by Wu and Squires[23] to a geometrically simple equilibrium three-dimensional TBL have provided further indication that LES and dynamic modeling may be a viable technique for prediction of complex spatially developing three-dimensional TBLs.

In addition to LES and dynamic modeling, RANS calculations offer another approach. Continuing improvements in closure models have in turn improved RANS capabilities. The v^2–f model developed by Durbin[24–26] has been used to accurately predict a range of

Received May 1, 1997; revision received Dec. 15, 1997; accepted for publication Dec. 22, 1997.

*Faculty Research Associate, Department of Mechanical and Aerospace Engineering, Box 876106.

†Associate Professor, Department of Mechanical and Aerospace Engineering, Box 876106.

equilibrium and nonequilibrium flows. This model was recently applied to prediction of the statistically two-dimensional TBL over a bump, shown in Fig. 1b (Ref. 27). The RANS predictions compared favorably with both LES results and the experimental measurements of Webster et al.[28] Aside from v^2–f, another closure gaining increased attention and use is the one-equation model developed by Spalart and Allmaras[29] (SA). In this approach a single transport equation is solved for the turbulent eddy viscosity. In Ref. 29, the model yields satisfactory predictions of several two-dimensional turbulent flows.

Both v^2–f and SA close the Reynolds stress using isotropic eddy viscosity. Although isotropic eddy viscosity models cannot capture the different directions of the shear stress and strain rate vectors in planes parallel to the wall, one interesting hypothesis discussed by Johnston and Flack[1] is that these models might still provide a practical approach for engineering calculation of three-dimensional TBLs. A model that can account for the different directions in stress and strain may not be crucial to obtaining an accurate prediction of the mean flow since turbulent shear stresses in the outer part of the boundary layer are typically small compared to pressure forces (see Ref. 1 for further discussion). Furthermore, in three-dimensional TBLs a quasicollateral region usually exists in the buffer layer within which the profile of the shear stress angle intersects that of the strain rate vector, i.e., there is an elevation at which the two vectors are colinear. From the intersection to the wall, the shear stress may even lead the strain rate, e.g., Refs. 1 and 30. Very close to the wall, the lead/lag of the shear stress will not be captured using isotropic eddy viscosity. However, this may not be a serious shortcoming because the magnitude of the turbulent shearing stresses in the viscous sublayer is small compared with the magnitude of the viscous stresses. Thus, the error associated with using isotropic eddy viscosity for calculation of three-dimensional TBLs may not result in significant inaccuracies in prediction of the mean flow. Application of accurate RANS models such as v^2–f and SA to a complex spatially developing three-dimensional TBL, therefore, has important implications for methods currently used in engineering calculations.

The primary objective of this work is to apply and compare LES and RANS predictions of a spatially developing three-dimensional TBL. The particular interest of this work is prediction of the flow over a bump swept at 45 deg with respect to the upstream two-dimensional boundary layer. The bump is formed by three tangential arcs (Fig. 1). A canonical zero-pressure gradient boundary layer at a momentum thickness Reynolds number $Re_{\theta,\mathrm{ref}} = 3.8 \times 10^3$ is introduced one-half chord length upstream of the onset of curvature. The boundary layer then experiences alternating signs of streamwise pressure gradient and surface curvature, as well as spanwise pressure gradient. The particular configuration shown in (Fig. 1) is considered because boundary-layer properties have been reported by Webster et al.[2] and provide a means for evaluation of simulation results. A suction slot parallel to the spanwise axis of the bump was used in the experiments to maintain a direction of statistical homogeneity, which in turn simplifies calculation of the flow. The governing equations, boundary conditions, and computational details for the RANS and LES calculations are presented in Secs. II.A and II.B, respectively. Comparisons of simulation results with the experimental measurements of Webster et al.[2] are given in Sec. III, followed by a summary and conclusions in Sec. IV.

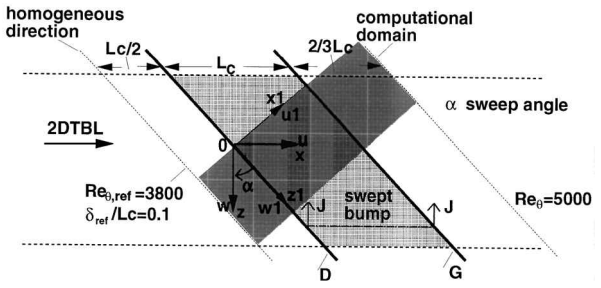

Fig. 1a Top view of the computational domain.

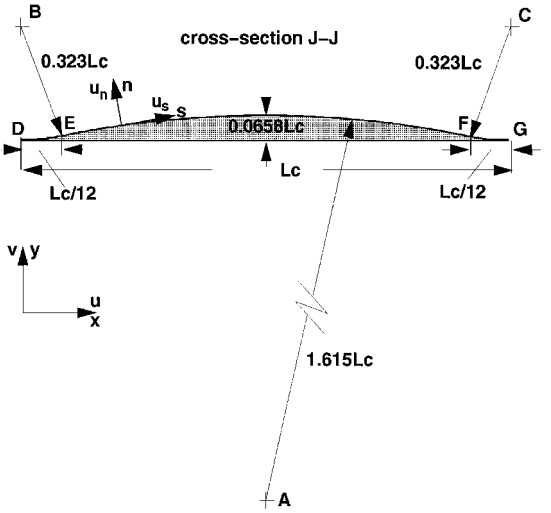

Fig. 1b Bump dimensions; D, E, F, and G, tangent points; upstream concave surface, $0 \le x/L_c \le \frac{1}{12}$; convex surface, $\frac{1}{12} \le x/L_c \le \frac{11}{12}$; downstream concave surface, $\frac{11}{12} \le x/L_c \le 1$.

II. Background

A. Simulation Overview for RANS

Time or ensemble averaging the equations of mass and momentum conservation yields the RANS equations

$$\mathrm{div}\langle \boldsymbol{u} \rangle = 0 \tag{1}$$

$$\frac{\partial \langle \boldsymbol{u} \rangle}{\partial t} + \mathrm{div}[\langle \boldsymbol{u} \rangle \langle \boldsymbol{u} \rangle] = -\mathrm{grad}\langle p \rangle + \mathrm{div}\left\{ \left(\frac{1}{Re} + \nu_t \right) [\mathrm{grad}\langle \boldsymbol{u} \rangle + (\mathrm{grad}\langle \boldsymbol{u} \rangle)^{\mathcal{T}}] \right\} \tag{2}$$

An eddy viscosity hypothesis has been used to close the Reynolds stresses, where ν_t is the turbulent eddy viscosity (the $\mathcal{T}$ superscript denotes the transpose). In Eqs. (1) and (2), $\langle \boldsymbol{u} \rangle$ is the mean velocity vector whose Cartesian components are $(\langle u \rangle, \langle v \rangle, \langle w \rangle)$. Velocities in Eqs. (1) and (2) are normalized by the inflow freestream value U_{ref} (subscript ref refers to quantities measured at the inlet station), lengths by the bump height h, and $Re = U_{\mathrm{ref}} h/\nu$, where ν is the kinematic viscosity.

In the v^2–f model, the turbulent eddy viscosity ν_t is evaluated from

$$\nu_t = C_\mu \langle v'^2 \rangle T \tag{3}$$

where T is the time scale defined as

$$T = \max\left[K/\varepsilon, 6(\nu/\varepsilon)^{\frac{1}{2}} \right] \tag{4}$$

The turbulence kinetic energy K, dissipation rate ε, and wall-normal fluctuation $\langle v'^2 \rangle$ appearing in Eqs. (3) and (4) are obtained through the following transport equations[24]:

$$\frac{\partial K}{\partial t} + \mathrm{div}[\langle \boldsymbol{u} \rangle K] = \mathcal{P} - \varepsilon + \mathrm{div}\left\{ \left(\frac{1}{Re} + \frac{\nu_t}{\sigma_K} \right) \mathrm{grad}\, K \right\} \tag{5}$$

$$\frac{\partial \varepsilon}{\partial t} + \mathrm{div}[\langle \boldsymbol{u} \rangle \varepsilon] = \frac{C_{\varepsilon 1}\mathcal{P} - C_{\varepsilon 2}\varepsilon}{T} + \mathrm{div}\left\{ \left(\frac{1}{Re} + \frac{\nu_t}{\sigma_\varepsilon} \right) \mathrm{grad}\, \varepsilon \right\} \tag{6}$$

$$\frac{\partial \langle v'^2 \rangle}{\partial t} + \mathrm{div}[\langle \boldsymbol{u} \rangle \langle v'^2 \rangle] = K f_{22} - \langle v'^2 \rangle \frac{\varepsilon}{K} + \mathrm{div}\left\{ \left(\frac{1}{Re} + \frac{\nu_t}{\sigma_K} \right) \mathrm{grad}\langle v'^2 \rangle \right\} \tag{7}$$

where f_{22} appearing in Eq. (7) is evaluated from

$$\frac{\partial f_{22}}{\partial t} = -(1 - C_1) \frac{\frac{2}{3} - \langle v'^2 \rangle / K}{T} + C_2 \frac{\mathcal{P}}{K} - f_{22} + C_L^2 l^2 \,\mathrm{div}(\mathrm{grad}\, f_{22}) \tag{8}$$

Note the use of a pseudo-time-derivativeterm in Eq. (8) so that the transport equations possess the same structure for numerical convenience, i.e., the left-hand side of Eq. (8) vanishes at convergence. The rate of turbulence kinetic energy production and the length scale l are given by

$$\mathcal{P} = \nu_t[\text{grad}\langle \boldsymbol{u}\rangle + (\text{grad}\langle \boldsymbol{u}\rangle)^{\mathcal{T}}]\text{grad}\langle \boldsymbol{u}\rangle$$

$$l^2 = \max\left[K^3/\varepsilon^2,\ C_3^2(\nu^3/\varepsilon)^{\frac{1}{2}}\right] \tag{9}$$

Model constants appearing in Eqs. (3–9) are the same as those in Ref. 24, i.e.,

$$C_\mu = 0.19, \qquad C_{\varepsilon 1} = 1.3 + 0.25/[1 + (n/2l)^2]^4, \qquad C_{\varepsilon 2} = 1.9$$
$$C_1 = 1.4, \qquad C_2 = 0.3, \qquad C_L = 0.3$$
$$C_3 = 70, \qquad \sigma_K = 1.0, \qquad \sigma_\varepsilon = 1.3$$

where n is the wall-normal distance as shown in Fig. 1b.

In the SA model, the turbulent eddy viscosity ν_t is evaluated from

$$\nu_t = \tilde{\nu} f_{\nu_1}, \qquad f_{\nu_1} = \frac{\chi^3}{\chi^3 + C_{\nu_1}^3}, \qquad \chi = \frac{\tilde{\nu}}{\nu} \tag{10}$$

The modified eddy viscosity $\tilde{\nu}$ is obtained from[29]

$$\frac{\partial \tilde{\nu}}{\partial t} + \text{div}[\langle \boldsymbol{u}\rangle \tilde{\nu}] = C_{b_1}\tilde{\Omega}\tilde{\nu} + \frac{C_{b_2}}{\sigma}|\text{grad}\,\tilde{\nu}|^2$$
$$- C_{w_1} f_w \left(\frac{\tilde{\nu}}{n}\right)^2 + \frac{1}{\sigma}\text{div}\left\{\left(\frac{1}{Re} + \tilde{\nu}\right)\text{grad}\,\tilde{\nu}\right\} \tag{11}$$

where

$$\tilde{\Omega} = |\text{curl}\,\boldsymbol{u}| + \frac{\tilde{\nu}}{\kappa^2 n^2} f_{\nu_2}, \qquad f_{\nu_2} = 1 - \frac{\chi}{1 + \chi f_{\nu_1}} \tag{12}$$

$$f_w = g\left[\frac{1 + C_{w_3}^6}{g^6 + C_{w_3}^6}\right]^{\frac{1}{6}}, \qquad g = r + C_{w_2}(r^6 - r)$$
$$r = \min\left[\frac{\tilde{\nu}}{\tilde{\Omega}\kappa^2 n^2}, 10\right] \tag{13}$$

Model coefficients appearing in Eqs. (10–13) are the same as in SA:

$$C_{b_1} = 0.135, \qquad \sigma = \tfrac{2}{3}, \qquad C_{b_2} = 0.622, \qquad \kappa = 0.41$$
$$C_{w_1} = C_{b_1}/\kappa + \left(1 + C_{b_2}\right)/\sigma, \qquad C_{w_2} = 0.3$$
$$C_{w_3} = 2, \qquad C_{\nu_1} = 7.1$$

The origin of the streamwise (x) coordinate is at the onset of curvature (Fig. 1). The bump chord/height ratio (L_c/h) is 15.2:1. The height of the computational domain is $\frac{2}{3}L_c$ measured from the flat plate ($y = 0$). The length of the upstream and downstream flat plates are $\frac{1}{2}L_c$ and $\frac{2}{3}L_c$, respectively. Because the flowfield is homogeneous along the coordinate parallel to the bump axis, RANS calculations were actually performed using dependent variables ($u1$, v, $w1$) in the ($x1$, y) plane (Fig. 1a). Results were then projected back to the laboratory (x, y) coordinate system.

No-slip conditions were applied on the wall for the velocity components, i.e., $\langle \boldsymbol{u}\rangle_w = 0$. For K, ε, $\langle v'^2\rangle$, f_{22}, and $\tilde{\nu}$, the boundary conditions on solid surfaces are

$$K_w = 0, \qquad \varepsilon_w = \frac{2\nu K_{n\to 0}}{n_{\to 0}^2} \tag{14}$$

$$\langle v'^2\rangle_w = 0, \qquad f_{22,w} = \frac{-20\nu^2\langle v'^2\rangle_{n\to 0}}{n_{\to 0}^4 \varepsilon_w}, \qquad \tilde{\nu}_w = 0 \tag{15}$$

(Note that the w subscript denotes values on the wall.)

At the inflow boundary, the profiles of the dependent variables were obtained from a separate precomputation of a flat plate boundary layer at $Re_\theta = 3.8\times 10^3$. At the exit plane, a convective boundary condition was used together with a correction on the streamwise velocity to ensure global mass conservation. Derivatives of K, ε, $\langle v'^2\rangle$, f_{22}, and $\tilde{\nu}$ along the $x1$ direction were assumed to be zero at the exit boundary. Over the top surface of the computational domain $\partial\langle u1\rangle/\partial y = 0$, $\langle v\rangle = 0$, $\partial\langle w1\rangle/\partial y = 0$, $\tilde{\nu} = 0$ were applied, while the derivatives of K, ε, $\langle v'^2\rangle$, and f_{22} along the y direction were assumed to be zero.

The numerical method adopted to solve the momentum and continuity equations (1) and (2) is the generalized fractional step method, e.g., Ref. 31. The computational domain is transformed from the Cartesian ($x1$, y) system to a body-fitted curvilinear system (ξ, η) where η is the coordinate normal to the flat plate. The dependent variable is transformed from ($u1$, v, $w1$) to a volume flux vector using area vectors. At each time step, transport equations for K, ε, $\langle v'^2\rangle$, f_{22}, or $\tilde{\nu}$ were solved using successive overrelaxation until the maximum residuals were reduced to machine zero. The grids were constructed so that the coordinate lines of constant ξ were perpendicular to the flat plate $y = 0$ and top surface of the computational domain. The grids were stretched only along the y direction. Grid independence was investigated through two calculations using the v^2–f model, referred to as RANS1 and RANS2. The grid size in RANS1 was 391 × 201, whereas in RANS2 196 × 101 grid points were used. Based on the friction velocity at the inlet, the spatial resolution was $\Delta x^+ = 90$ for RANS1 and $\Delta x^+ = 180$ for RANS2, respectively. For both calculations the first grid point normal to the wall was approximately one wall unit from the lower surface. The same grid used in RANS2 was also employed in a calculation using the SA model, which is referred to as RANS3.

Using the inlet profile as initial condition, the system of Eqs. (1) and (2) and (5–8) [or Eq. (11)] was advanced to steady state. The flow was considered converged when the following criteria were satisfied:

$$\max\left\{\frac{|\langle u1\rangle(x1, y, t) - \langle u1\rangle(x1, y, t - 10\delta_{\text{ref}}/U_{\text{ref}})|}{U_{\text{ref}}}\right\} < 10^{-5} \tag{16}$$

$$\max\left\{\frac{|\langle v\rangle(x1, y, t) - \langle v\rangle(x1, y, t - 10\delta_{\text{ref}}/U_{\text{ref}})|}{U_{\text{ref}}}\right\} < 10^{-6} \tag{17}$$

$$\max\left\{\frac{|K(x1, y, t) - K(x1, y, t - 10\delta_{\text{ref}}/U_{\text{ref}})|}{U_{\text{ref}}^2}\right\} < 10^{-6} \tag{18}$$

$$\max\left\{\frac{|\langle v'^2\rangle(x1, y, t) - \langle v'^2\rangle(x1, y, t - 10\delta_{\text{ref}}/U_{\text{ref}})|}{U_{\text{ref}}^2}\right\} < 10^{-6} \tag{19}$$

B. Simulation Overview for LES

In LES, mass and momentum conservation are enforced for the large-scale resolved variables, which are obtained by filtering the Navier–Stokes equations

$$\text{div}\,\bar{\boldsymbol{u}} = 0 \tag{20}$$

$$\frac{\partial \bar{\boldsymbol{u}}}{\partial t} + \text{div}(\bar{\boldsymbol{u}}\bar{\boldsymbol{u}}) = -\text{grad}\,\bar{p}$$
$$+ \text{div}\left\{\left(\frac{1}{Re} + \nu_{\text{SGS}}\right)[\text{grad}\,\bar{\boldsymbol{u}} + (\text{grad}\,\bar{\boldsymbol{u}})^{\mathcal{T}}]\right\} + \mathcal{E}_c \tag{21}$$

where an eddy viscosity hypothesis has been used to close the subgrid stress and ν_{SGS} is the SGS eddy viscosity. In Eqs. (20) and (21) an overbar denotes the filtered variable. The term $\mathcal{E}_c$ appearing in Eq. (21) is the commutation error because, in general the filtering operation does not commute with differentiation. As shown in Ref. 32, the commutation error is second order in the filter width. For calculation of spatial derivatives using approximations that are second-order accurate, as in the present work, filtering can be assumed to commute with differentiation. Therefore, $\mathcal{E}_c$ is neglected in this study (see Ref. 32 for further discussion).

The eddy viscosity in Eq. (21) is expressed as[16]

$$\nu_{\text{SGS}} = C\bar{\Delta}^2|\bar{\boldsymbol{S}}| = C\bar{\Delta}^2\sqrt{2\boldsymbol{S}\boldsymbol{S}} \tag{22}$$

where $|\bar{\boldsymbol{S}}|$ is the magnitude of the large-scale strain rate tensor $\boldsymbol{S} = [\text{grad}\,\bar{\boldsymbol{u}} + (\text{grad}\,\bar{\boldsymbol{u}})^{\mathcal{T}}]/2$.

Following Germano et al.,[14] a second filter, the test filter (denoted by a caret) is used to derive an expression for the model coefficient C:

$$C = -\frac{1}{2}\frac{L_{ij}M_{ij}}{M_{ij}M_{ij}} \tag{23}$$

where

$$M_{ij} = \hat{\bar{\Delta}}^2|\hat{\bar{S}}|\hat{\bar{S}}_{ij} - \bar{\Delta}^2\widehat{|\bar{S}|\bar{S}_{ij}}, \qquad L_{ij} = \widehat{\bar{u}_i\bar{u}_j} - \hat{\bar{u}}_i\hat{\bar{u}}_j \tag{24}$$

where the least-squares approach of Lilly[33] has been used to obtain Eq. (23). The filter widths at the subgrid and subtest levels are denoted $\bar{\Delta}$ and $\hat{\bar{\Delta}}$, respectively.

In the results presented in this paper, the model coefficient is calculated by averaging the numerator and denominator in Eq. (23) over the homogeneous spanwise direction to eliminate numerical instabilities arising from small values of the denominator. Ghosal et al.[18] showed that Eq. (23), with averaging of the numerator and denominator, can be rigorously derived by constraining C to have no variation along directions of spatial homogeneity (also see Ref. 17). Therefore, the coefficient C is time dependent and a function of the two inhomogeneous coordinates. A clipping function was used to ensure nonnegative values of C following the spanwise averaging applied to Eq. (23). The test filtering operation was performed in physical space on the coordinate plane $\eta = \text{const}$ using a tophat filter of width equal to two mesh spacings. Test filtering is performed numerically by applying Simpson's rule of integration. At the end of each time step, the Cartesian velocity components $(\overline{u1}, \bar{v}, \overline{w1})$ are recovered to compute the model coefficient C and SGS eddy viscosity using the procedure given in Eqs. (22–24). The reader is referred to Ref. 34 for further discussion of issues related to filtering in complex domains.

Measurements from Webster et al.[2] showed that the bump caused a relatively small distortion of the flow at a location one-half chord length upstream of the onset of curvature ($x/L_c = -\frac{1}{2}$ in Fig. 1). To compare LES predictions to experimental measurements, it is necessary to specify in the simulations a realistic, two-dimensional boundary layer at the same location. In the current study, a time-dependent velocity field at the inflow boundary was obtained through a separate LES precalculation of a flat plate boundary layer over a continuous momentum thickness Reynolds number range $3.6 \times 10^3 \le Re_\theta \le 4.2 \times 10^3$ (Refs. 35 and 36). After a statistically steady state had been achieved, the three velocity components at a streamwise station $Re_\theta = 3.8 \times 10^3$ were stored for $300\delta_{\text{ref}}/U_{\text{ref}}$ at a time step $dt = 0.01\delta_{\text{ref}}/U_{\text{ref}}$ and were subsequently fed to the inlet ($x/L_c = -\frac{1}{2}$) of the spatially developing bump flow simulation. As in the experiments of Webster et al.,[2] the inlet boundary-layer thickness $\delta_{\text{ref}} = 1.5h$. Boundary conditions applied on the top and exit planes are essentially similar to those described in Sec. II.A for the RANS calculations. Periodic boundary conditions were applied in the spanwise direction.

In the LES, the near-wall flow ($0 \le y^+_{\text{ref}} \le 25$) was modeled using approximate boundary conditions similar to those previously employed by Schumann,[37] Piomelli et al.,[38] and Cabot.[39] In particular, the instantaneous wall stress is assumed to be in phase with and proportional to the local LES velocity at the first plane of grid points nearest the wall. The instantaneous wall stresses $\tau_{s,w}$ and $\tau_{z1,w}$ are calculated from

$$\tau_{s,w} = \frac{\bar{u}_s(x1, y, z1, t)}{\langle\bar{u}_s\rangle(x1, y, t)}\langle\tau_{s,w}\rangle, \qquad \tau_{z1,w} = \frac{\overline{w1}(x1, y, z1, t)}{\langle\overline{w1}\rangle(x1, y, t)}\langle\tau_{z1,w}\rangle \tag{25}$$

where the mean wall shear stresses $\langle\tau_{s,w}\rangle$ and $\langle\tau_{z1,w}\rangle$ were prescribed through interpolation of the experimental skin-friction data of Webster et al.[2] or the RANS3 results using the SA model. The mean velocities $\langle\bar{u}_s\rangle(x1, y, t)$ and $\langle\overline{w1}\rangle(x1, y, t)$ are obtained by performing spanwise averaging at each time step during the calculation.

It is important to note that, by construction, calculations performed using the boundary conditions (25) do not predict the mean skin friction because this quantity is input to the calculation. However, using Eq. (25) together with a priori input of the mean stress circumvents the need to assume the near-wall flow satisfies a universal profile, e.g., a log law. The calculations are then useful for gauging the accuracy of the LES in the outer (resolved) part of the flow, using a simple (equilibrium-based) prescription of the wall stress.

The numerical approach used to solve the continuity and momentum equations (20) and (21) is the same as that described in Sec. II.A. LES calculations were performed using two grid sizes, $586 \times 51 \times 65$ (referred to as LES1) and $391 \times 51 \times 33$ (referred to as LES2) in the streamwise, wall-normal, and spanwise directions, respectively. Based on the friction velocity at the inlet, the spatial resolution in LES1 is $\Delta x^+ = 60, \Delta y^+_{\text{min}} > 25$, and $\Delta z^+ = 38$. In LES2 the spatial resolution is $\Delta x^+ = 90, \Delta y^+_{\text{min}} > 25$, and $\Delta z^+ = 76$. In both LES1 and LES2, the experimentally measured skin friction was used to prescribe the mean wall shear stresses in the approximate boundary condition (25). Calculations of the boundary layer over the unswept bump showed LES predictions obtained using the mean friction from a v^2–f calculation in Eq. (25) yielded similar results to those in which the experimentally measured skin friction was employed in the approximate boundary conditions.[27] The sensitivity of LES predictions of the outer (resolved) flow to the mean wall shear in Eq. (25) is examined in this study in a calculation (referred to as LES3), in which the mean wall shear stress components in Eq. (25) were prescribed using the RANS3 prediction obtained using the SA model. The impact of the spanwise dimension of the computational domain on LES predictions is also considered in LES3 ($391 \times 51 \times 65$). The spanwise length was doubled from $0.2L_c$ in LES2 to $0.4L_c$ in LES3, while maintaining the same resolution. Using the inlet profile at $t = 0$ as the initial condition, the flow was allowed to evolve for $100\delta_{\text{ref}}/U_{\text{ref}}$ at a time step $dt = 0.01\delta_{\text{ref}}/U_{\text{ref}}$, and statistics were then collected for a period of $200\delta_{\text{ref}}/U_{\text{ref}}$. Turbulence statistics in the (x, y, z), $(x1, y, z1)$, and (n, s, z) coordinate systems were obtained using standard tensor algebra operations.

III. Results

The surface static pressure coefficient C_{pw} $(= (\langle\bar{p}_w\rangle - \langle\bar{p}_{w,\text{ref}}\rangle)/\frac{1}{2}U^2_{\text{ref}})$ is compared with the experimental measurements of Webster et al.[2] in Fig. 2a. Figure 2a shows the streamwise pressure gradient, dC_{pw}/ds, which undergoes quasistep changes near the leading and trailing edge of the bump, where the surface curvature also changes sign. Because the flow remains homogeneous along the coordinate

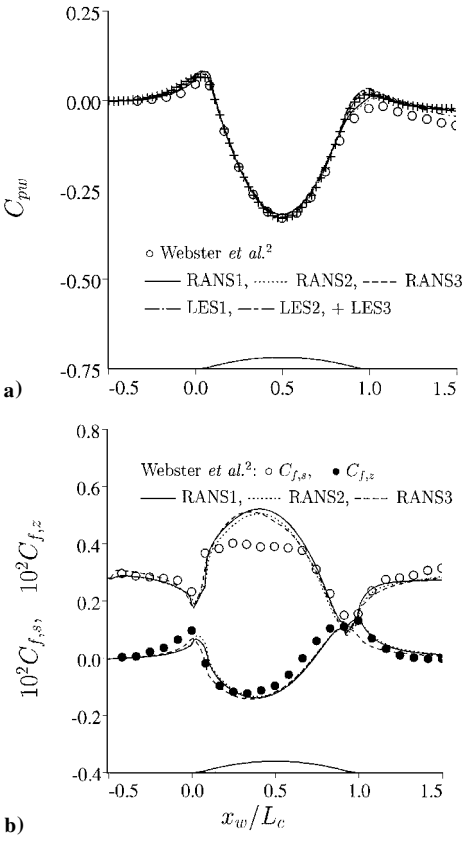

Fig. 2 Wall static pressure coefficient and skin-friction coefficients: a) C_{pw} and b) $C_{f,s}$ and $C_{f,z}$.

parallel to the bump axis, the spanwise pressure gradient $\partial C_{pw}/\partial z$ can be inferred from the streamwise value, i.e., $\partial C_{pw}/\partial z = -\partial C_{pw}/\partial x \tan\alpha$. Thus, both the streamwise and spanwise pressure gradients experience three sign changes over the bump surface.

Overall, there is reasonable agreement between the simulations and experiment. RANS1 and RANS2 predictions obtained using two different grid sizes collapse, indicating adequate resolution and grid independence in calculation of C_{pw}. LES predictions using different spanwise sizes and grid resolutions also collapse, with the exception of a slightly improved prediction near the downstream boundary for LES1 at the finer resolution. Near the trailing edge ($x_w/L_c = 1$), LES results are over the measurements. The overprediction may be because, near the trailing edge, the near-wall flow is strongly skewed away from the streamwise direction, e.g., see Figs. 2b and 3. Previous LES results obtained in the (statistically) two-dimensional TBL over the unswept bump are not overpredicted near the trailing edge.[27] The strong turning of the flow could interact with the streamwise acceleration/deceleration, resulting in a slightly different C_{pw} compared to measurements. In addition, the pressure used in forming C_{pw} in the LES is that at the first layer of pressure points nearest, but not at, the wall. Correcting for the wall-normal variation, especially in regions of strong adverse pressure gradient such as occurring near the trailing edge, might also improve the agreement.

Simulation results and experimental measurements of the streamwise, $C_{f,s}$, and spanwise, $C_{f,z}$, skin-friction coefficients are compared in Fig. 2b. Note because the mean wall shear stress components in the approximate boundary condition (25) were prescribed in LES1 and LES2 using the experimental data, and in LES3 using the RANS3 results, the mean friction is not predicted in the present LES. The variations in the predicted skin-friction from RANS1 to RANS2 (grid resolution being coarsened by factor of two) are negligible. Except for the distributions near the summit and, to a lesser extent, in the downstream recovery region, the streamwise skin-friction coefficient $C_{f,s}$ obtained using the v^2–f and SA models are in good agreement with the experimental measurements of Webster et al.[2] The overprediction near the summit is not related to effects of mean-flow three dimensionality because it is also present in calculations of the companion two-dimensional (unswept) flow.[27] Webster et al.[2] attributed the plateau in the skin friction between $0.1 < x_w/L_c < 0.7$ to the early stages of boundary-layer relaminarization. RANS predictions of the spanwise skin-friction coefficient $C_{f,z}$ are in excellent agreement with the experimental measurements of Webster et al.[2] The alternating spanwise pressure gradient skews the near-wall flow and results in two sign changes in $C_{f,z}$. Over the upstream flat plate, fluid particles near the wall are deflected toward the positive z direction (cf., Figs. 1 and 3). This positive skewing is reversed over the bump surface upstream of the summit by a positive spanwise pressure gradient, as evident in the negative values in $C_{f,z}$ near the summit. Near the trailing edge, fluid particles are strongly skewed toward the positive z direction. Note that, in this region very close to the wall, $\tan[\langle w\rangle/\langle u_s\rangle] = \tan[C_{f,z}/C_{f,s}] > 1$, indicating the near-wall streamlines are skewed more than 45 deg, as also shown in Fig. 3b. The present flow is, therefore, strongly turned, e.g., in Ref. 3 the wall shear stress is turned by about 30 deg on an infinite swept wing.

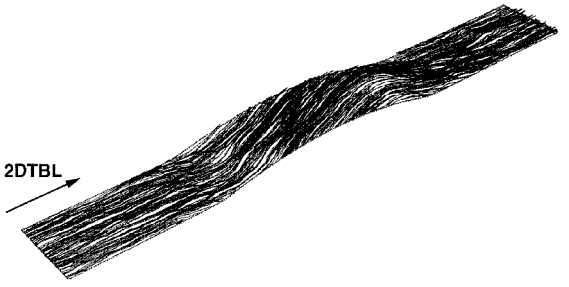

Fig. 3a Perspective view of instantaneous streamlines near the plane of $y/\delta_{ref} = 0.05$ (LES1).

Profiles of the mean horizontal velocity $\langle\bar{u}\rangle$ and mean spanwise velocity $\langle\bar{w}\rangle$ at six streamwise locations are compared with the experimental measurements of Webster et al.[2] in Fig. 4. The first station ($x/L_c = -\frac{1}{2}$) is at the inflow boundary, and the next five stations are on the downstream side of the bump. (Aside from the inlet, no measurements were made upstream of the bump summit.) The velocity profiles are normalized by the local edge velocity U_e, which is defined as the maximum along each vertical traverse.[2] The vertical coordinate is normalized by the corresponding boundary-layer thickness δ_{U_e}. The collapse of LES1 and LES2 predictions shows that the mean flow is well resolved. Results from RANS1 and RANS2 calculations are also identical, indicating adequate resolution and grid independence in the mean flow.

Overall, LES and RANS predictions of the mean streamwise and spanwise velocities are in very good agreement with the experimental measurements. The significant streamwise variations in the mean horizontal velocity and the sign reversal in the mean spanwise velocity have been accurately captured by both techniques. The largest discrepancies occur near the trailing edge of the bump ($x/L_c = 1$), where the mean streamwise velocity $\langle\bar{u}\rangle$ in the v^2–f calculation is slightly less accurate than from the other techniques (LES and RANS using SA). On the other hand, the v^2–f model yields an excellent prediction of the mean spanwise velocity at all six stations, whereas the LES calculations underpredict this quantity. The cause for the underprediction in $\langle\bar{w}\rangle$ is probably the use of approximate boundary conditions in the LES because the peak of $\langle\bar{w}\rangle$ is determined by the combined effects of the no-slip condition and spanwise pressure gradient. The no-slip condition is not enforced for the spanwise velocity, i.e., the approximate boundary condition is applied to determine the shear stress.

The sign changes in the mean crossflow velocity $\langle\bar{w}\rangle$ with streamwise distance evident in Fig. 4 are consistent with the skewing angle of the mean flow shown in Fig. 3b. It is also interesting that Fig. 3b shows that along the bump surface there exist two regions where $\langle\bar{w}\rangle$ reverses sign along the wall-normal coordinate. This is consistent with the S-shaped crossflow profile discussed by Johnston and Flack[1] and occurs because the near-wall flow is turned more quickly by the spanwise pressure gradient than the outer flow. The peak of the mean crossflow velocity is about 20% of the freestream velocity, comparable to the values in other experiments on three-dimensional TBLs. In general, compared to previous results obtained by Wu and Squires[27] in the two-dimensional flow over the bump (zero sweep angle), the quality of the mean velocities predicted in both the LES and RANS in the three-dimensional TBL is comparably good. Although not shown here, LES and RANS predictions of the mean vertical velocity $\langle\bar{v}\rangle$ are also accurate compared with the experimental measurements of Webster et al.[2]

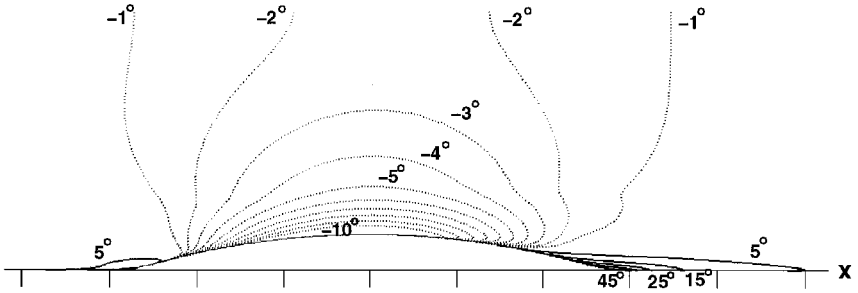

Fig. 3b Mean velocity skewing angle atan $\langle w\rangle/\langle u_s\rangle$ (RANS1).

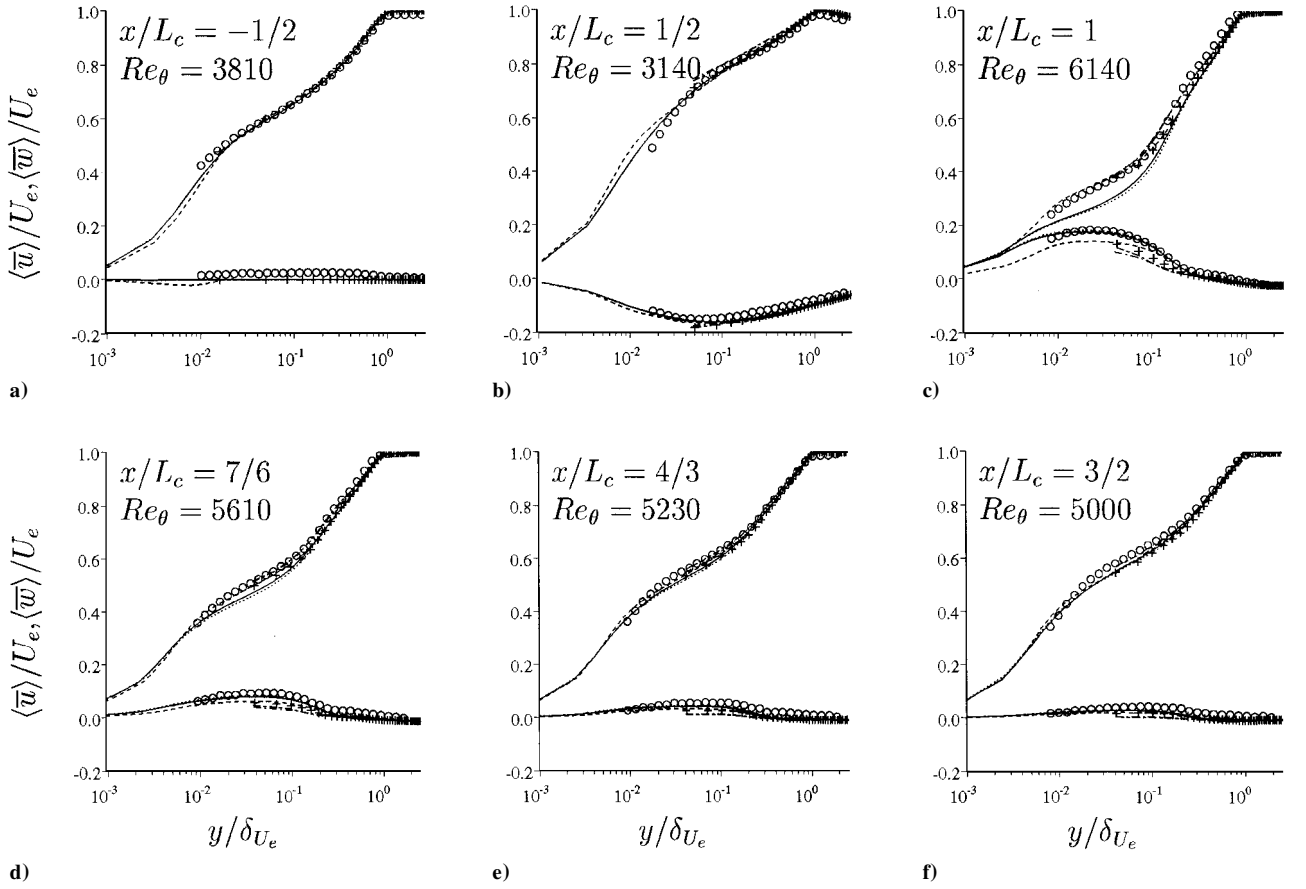

Fig. 4 Mean velocity components $\langle\bar{u}\rangle/U_e$ and $\langle\bar{w}\rangle/U_e$ along vertical traverses: ∘, Webster et al.[2]; ——, RANS1; - - - -, RANS2; – – –, RANS3; — - —, LES1; — – — LES2; and +, LES3.

The accurate prediction of the mean flow (both streamwise and spanwise) obtained using an isotropic eddy viscosity model in the RANS calculation is interesting. One possible explanation is that the model accurately predicts the three-dimensional TBL because boundary-layer distortion resulting from the crossflow is relatively weak compared to other effects, e.g., streamwise pressure gradient. A related issue is then whether the deformation by the crossflow in the flow over the bump is weak relative to other three-dimensional TBLs. One approach to shedding light on these issues is through examination of the strain rate. Relevant is the recent work by Coleman et al.[11] in which DNS was used to investigate the effect of deformations typical to spatially developing three-dimensional TBLs. Coleman et al.[11] prescribed elements of the deformation tensor to simulate the flow over an infinite swept wing, e.g., Ref. 3. Lateral irrotational skewing ($\partial\langle w\rangle/\partial x = \partial\langle u\rangle/\partial z$), together with streamwise deceleration ($\partial\langle u\rangle/\partial x < 0$, $\partial\langle v\rangle/\partial y > 0$), was applied to a fully developed channel flow. Coleman et al.[11] found the flow was more sensitive to streamwise strains than those due to the three-dimensional skewing. Their findings are consistent with the measurements of Webster et al.,[2] where structural parameters such as the stress-intensity ratio in the three-dimensional TBL over the swept bump were not markedly different from those in the two-dimensional boundary layer.

In the flow over the bump, the deformations corresponding to those in three-dimensional TBLs over infinite swept wings occur downstream of the summit, where an adverse pressure gradient prevails. This may be observed in Figs. 5 and 6, where the nondiagonal and diagonal components of the normalized strain rate tensor, $S_{ij}/|\boldsymbol{S}|$, are shown. The strain rates shown in Figs. 5 and 6 were obtained from the RANS1 calculation. Figure 5a shows contours of the primary strain rate S_{12}, which acts in the streamwise (x, y) plane. As shown in Fig. 5a, S_{12} remains positive inside the boundary layer because $\langle u\rangle$ monotonically increases toward the boundary-layer edge and the flow remains attached, i.e., $\langle u\rangle > 0$. Although, in general, the magnitude of S_{12} is larger than the other two off-diagonal components, the S_{23} component, which acts in the transverse (y, z) plane, is comparable to S_{12} in three regions, i.e., near the leading edge, at the summit, and at the trailing edge (Fig. 5b). This is due to the strong spanwise skewing occurring in these regions, as earlier shown in the distributions of $C_{f,z}$ and mean-flow skewing angle. Typical of crossflow profiles in pressure-driven flows, Fig. 5b shows that, away from the wall, S_{23} has opposite sign to that of the mean spanwise velocity because $\langle w\rangle$ decreases with increasing y. The sign of S_{23} reverses in the immediate neighborhood of the surface because the no-slip boundary condition forces an increase in $\langle w\rangle$ with distance from the wall.

The two diagonal components S_{11} and S_{22} in Figs. 6a and 6b reflect the acceleration/deceleration caused by the streamwise pressure gradient, whereas the other diagonal component S_{33} shown in Fig. 6b reflects the spanwise stretching/compression due to the spanwise pressure gradient, e.g., see Ref. 11. Over the rear surface of the bump, the strong adverse pressure gradient results in $S_{11} < 0$ and $S_{22} > 0$. The magnitudes of the three diagonal components are also comparable. Because the flow is homogeneous in the coordinate parallel to the bump axis, $\partial\langle w\rangle/\partial x = -\partial\langle w\rangle/\partial z/\tan\alpha$ and $\partial\langle u\rangle/\partial z = -\partial\langle u\rangle/\partial x \tan\alpha$. Thus, for $\alpha = 45$ deg, the off-diagonal component S_{13} in Fig. 5c is related to the diagonal components S_{11} and S_{33} as $S_{13} = -(S_{11} + S_{33})/2$. In Ref. 11, the diagonal and off-diagonal deformations were prescribed to simulate the flow over a 45-deg infinite swept wing, with the same relationship between S_{13}, S_{11}, and S_{33}. In their work,[11] the mean deformations were prescribed as $S_{22} = -2S_{11} = -2S_{33} = 2S_{13}$. In the flow over the bump, similar relationships between the diagonal and off-diagonal components are shown in Figs. 6a and 6b and Fig. 5c, e.g., over the rear bump surface (downstream of the summit) in the region where $0.08 < S_{22}/|S| < 0.16$ (Fig. 6b), $-0.12 < S_{11}/|S| < -0.08$ (Fig. 6a), and $0.04 < S_{13}/|S| < 0.08$ (Fig. 5c). Based on the results shown in Figs. 5 and 6, the infinite swept wing considered by Coleman et al.[11] is similar to the three-dimensional TBL over the bump in that they possess similar deformations. In that sense, the flow over the swept

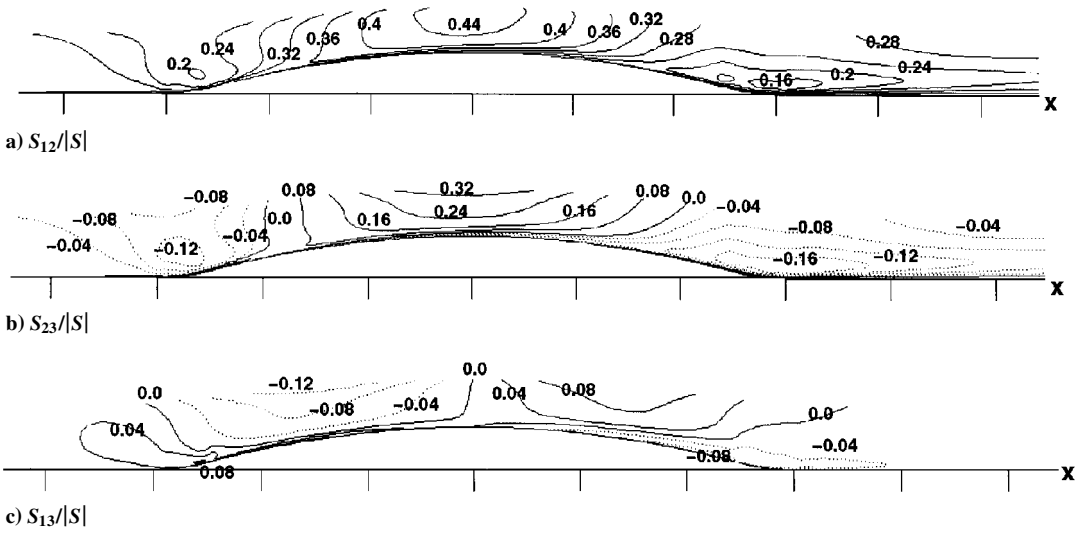

Fig. 5 Normalized nondiagonal components of the strain rate tensor S_{ij}.

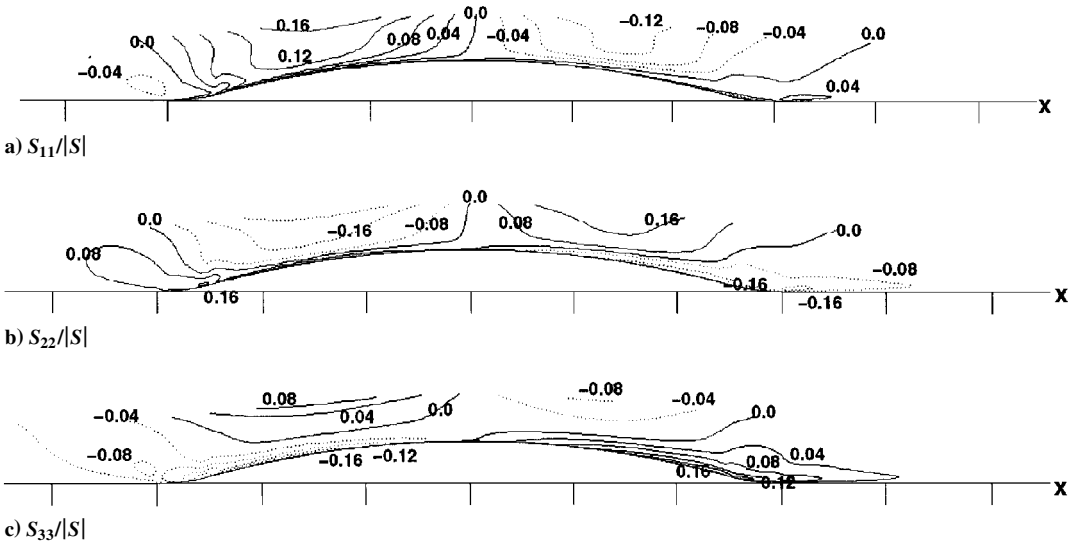

Fig. 6 Normalized diagonal components of the strain rate tensor S_{ij}.

bump is a representative case among a class of spatially developing three-dimensional TBLs that arise in infinite geometries.

Predictions of the turbulence kinetic energy are compared with the experimental measurements in Fig. 7. Overall, LES predictions are in very good agreement with the experimental data of Webster et al.,[2] accurately capturing the distortion of the turbulence kinetic energy over the bump surface and recovery over the trailing flat plate. LES1 results using a finer resolution are only slightly higher than those obtained from LES2, indicating that turbulence fluctuations in the region of $y^+_{\text{ref}} > 25$ have been reasonably well resolved using grid spacings of $\Delta x^+ = 90$ and $\Delta z^+ = 76$. Figure 7 also shows LES3 predictions of K obtained using the RANS3 prediction of the mean wall shear stress in the approximate boundary conditions. As shown in Fig. 7 the perturbation applied to Eq. (25) via an incorrect description of the mean stress does not have an overly adverse effect on LES predictions of the outer flow. As also observed in the unswept bump,[27] these features demonstrate that LES predictions of the three-dimensional TBL over the bump are relatively insensitive to the specific prescription of the mean wall shear stress in Eq. (25). The agreement between RANS predictions of the turbulence kinetic energy and the experimental measurements of Webster et al.[2] is reasonable, with some overpredictions as evident in Fig. 7. Interestingly, the inner peak at $x/L_c = 1$ arising from the generation of an internal layer is at least partially captured in the RANS calculations.

Resolved turbulent shear stress components $-\langle\bar{u}'\bar{v}'\rangle$, $-\langle\bar{v}'\bar{w}'\rangle$, and $-\langle\bar{u}'\bar{w}'\rangle$ are compared to those of Webster et al.[2] in Fig. 8. Figure 8a shows the primary shear stress profiles from the LES precomputations used to generate the inflow condition are in good agreement with that measured by Webster et al.[2] with a small overprediction of the peak. At the other five stations, the agreement between LES predictions and measurements of $-\langle\bar{u}'\bar{v}'\rangle$ and $-\langle\bar{v}'\bar{w}'\rangle$ is excellent. Also evident is that the other secondary shear stress $-\langle\bar{u}'\bar{w}'\rangle$ is overpredicted near the bump trailing edge ($x/L_c = 1$ and $\frac{7}{6}$). In the boundary-layer approximation, this stress is neglected because it does not enter into the transport equations of the mean streamwise and spanwise velocity, e.g., see Johnston and Flack.[1] The figure shows a slight increase in $-\langle\bar{u}'\bar{v}'\rangle$ in LES1 compared to that in LES2, consistent with the finer resolution used in LES1. At the summit, the LES correctly predicts the sharp reduction in the shear stresses by convex curvature and favorable pressure gradient. On the downstream side of the bump in the region of strong adverse pressure gradient there is a significant increase in both components near the wall. Over the downstream flat plate, LES predictions of the recovery of the shear stress profiles are in good agreement with the experimental measurements of Webster et al.[2] As the boundary layer relaxes over the trailing flat plate after the removal of curvature and pressure gradients, the high peak in the $-\langle\bar{u}'\bar{v}'\rangle$ profile attained at $x/L_c = 1$ decays rapidly as evident in Figs. 8d–8f.

Properties of the dynamic eddy viscosity model are presented in Fig. 9. Figure 9a shows the model coefficient C defined in Eq. (23) after time and spanwise averaging. The profiles indicate at the bump summit there is a reduction in C due to the stabilizing effects of favorable pressure gradient and convex curvature. The reduction is also evident in the profiles of the eddy viscosity, ν_{SGS}, and dissipation

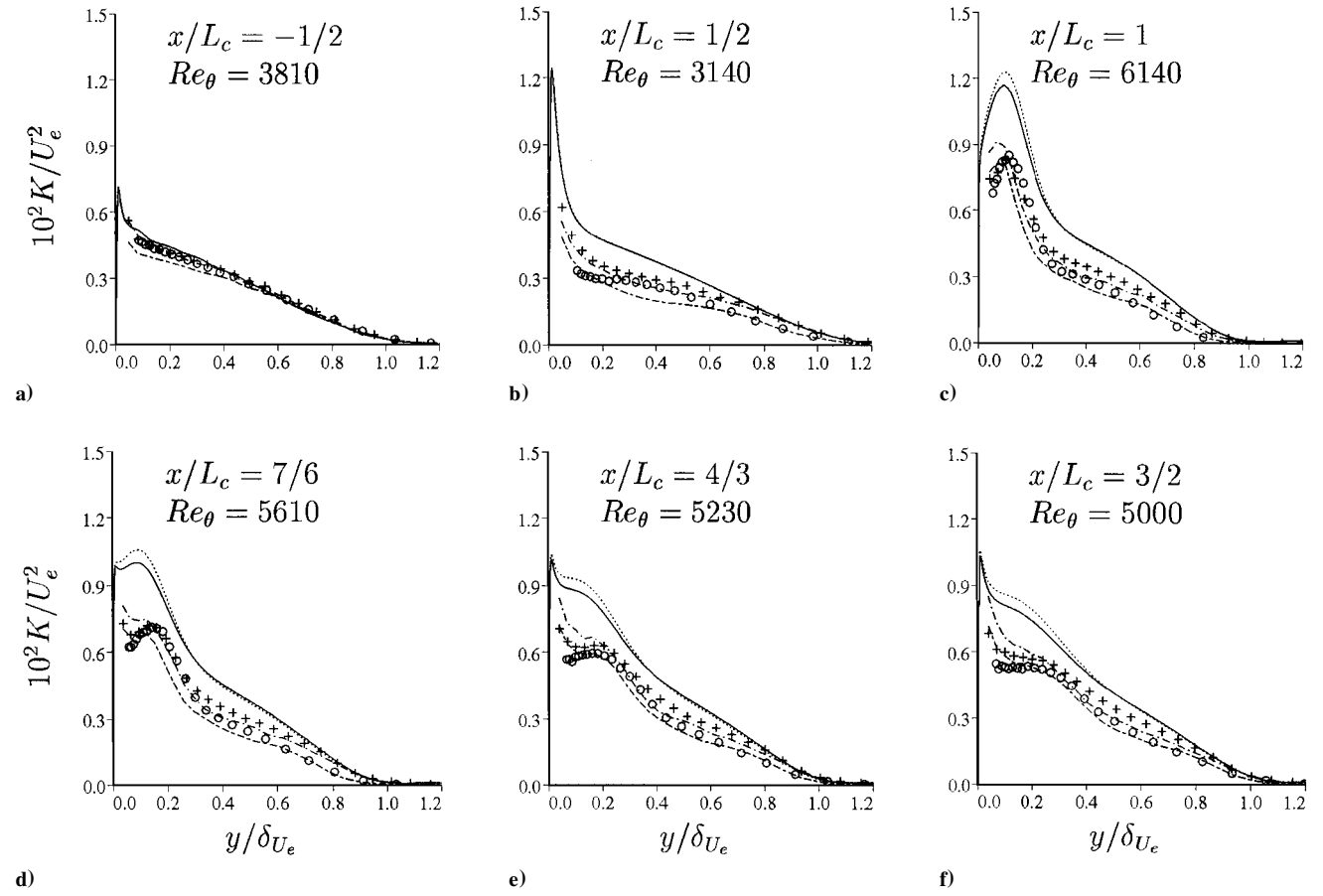

Fig. 7 Turbulence kinetic energy along vertical traverses: ∘, Webster et al.[2]; ——, RANS1; - - - -, RANS2; — - —, LES1; — – —, LES2; and +, LES3.

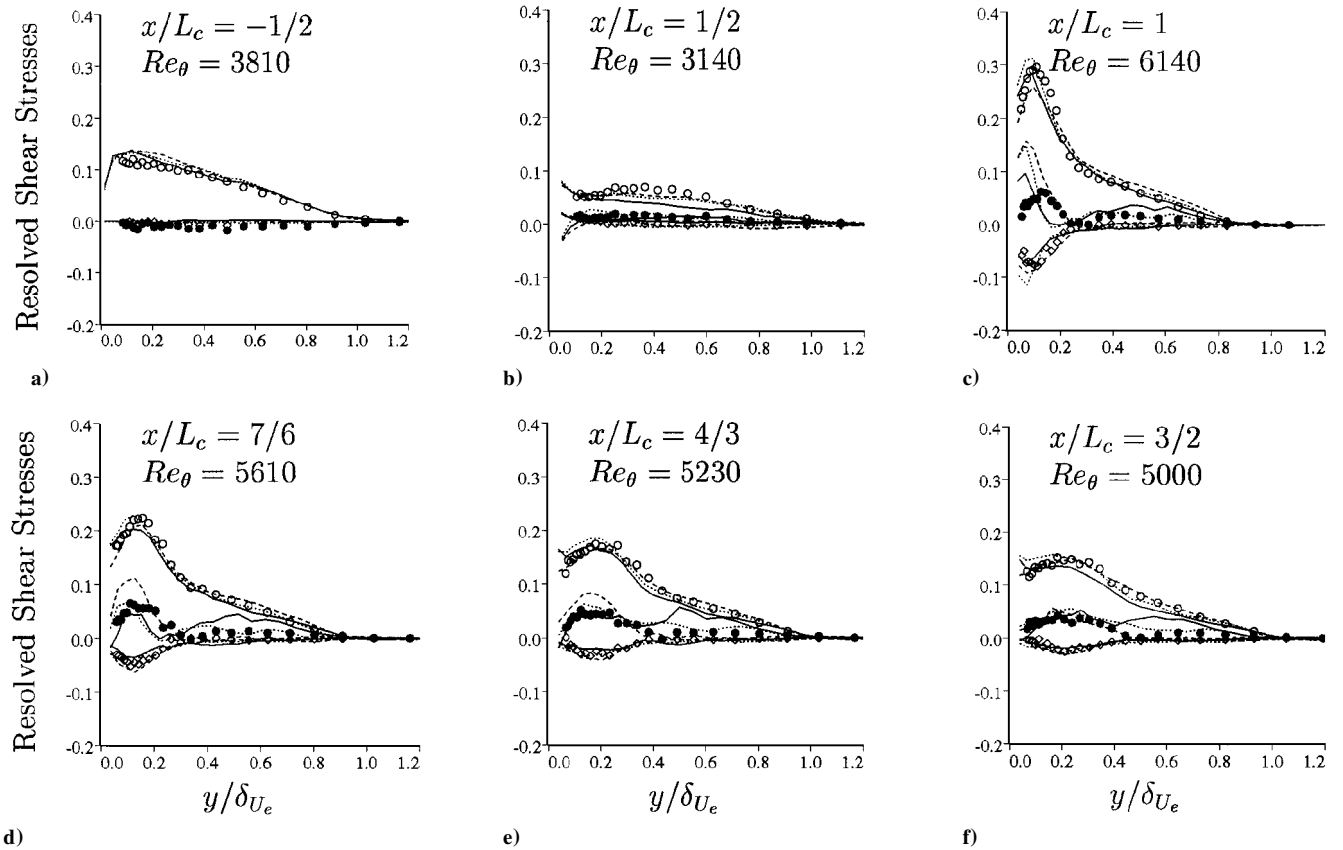

Fig. 8 Resolved turbulent shear stress: ——, LES1; - - - -, LES2; – – –, LES3; ∘, $-10^2\langle\tilde{u}'\tilde{v}'\rangle/U_e^2$; ◇, $-10^2\langle\tilde{v}'\tilde{w}'\rangle/U_e^2$; and ●, $-10^2\langle\tilde{u}'\tilde{w}'\rangle/U_e^2$ (symbols, Webster et al.[2]).

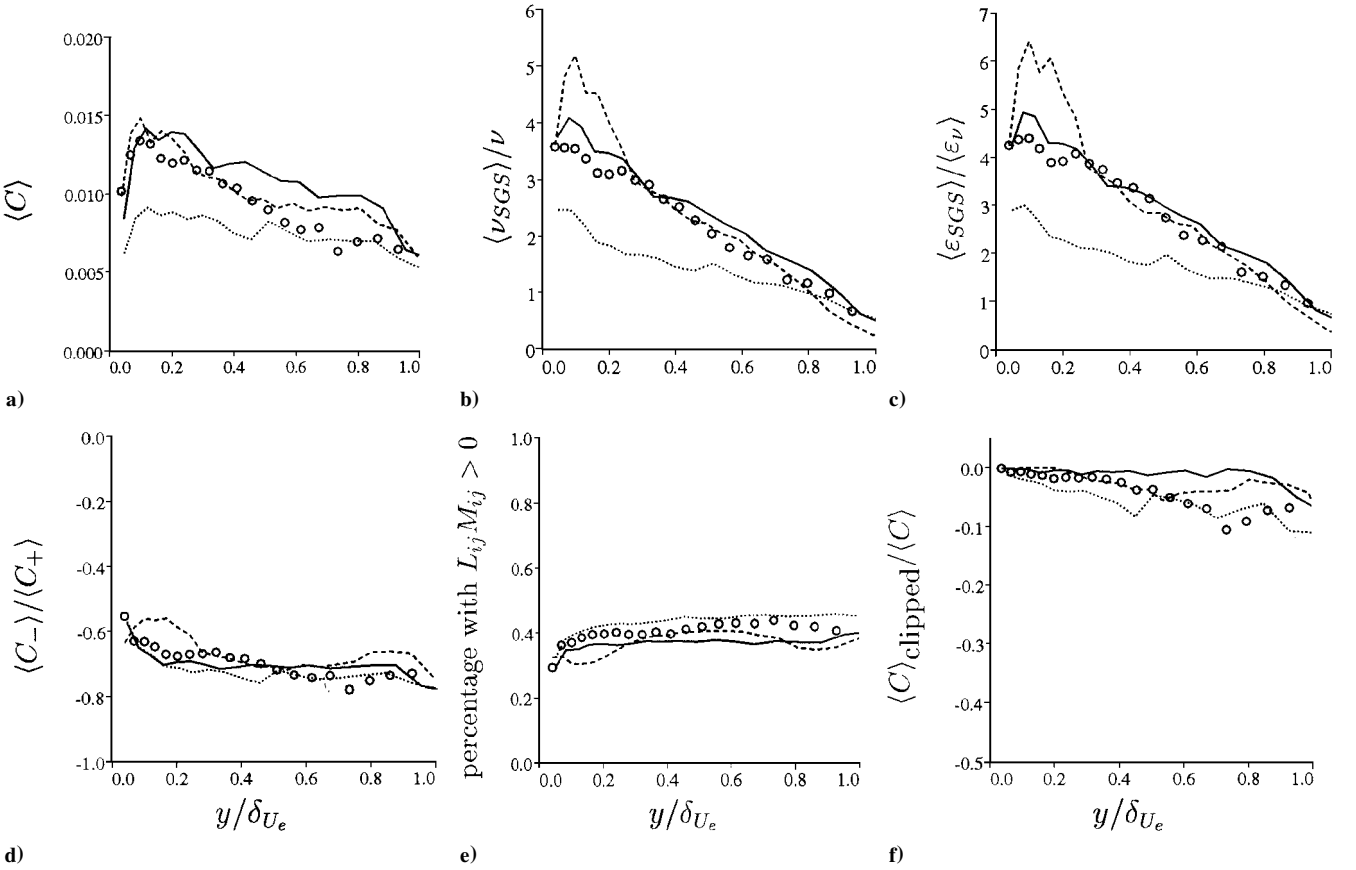

Fig. 9 SGS model properties from LES3: ——, $x_w/L_c = -\frac{1}{2}$; - - - -, $\frac{1}{2}$; – – –, 1; and ∘, $\frac{3}{2}$; a) averaged model coefficient, b) ratio of eddy to molecular viscosity, c) ratio of SGS to molecular dissipation, d) ratio of averaged backward and forward contributions to model coefficient, e) percentage of points with $L_{ij}M_{ij} > 0$ corresponding to locally negative C, and f) ratio of clipped negative model coefficient (after spanwise averaging) and the model coefficient.

rate, $\varepsilon_{\mathrm{SGS}}$ $(= -\tau_{ij}\bar{S}_{ij})$, shown in Figs. 9b and 9c. At $x_w/L_c = \frac{1}{2}$, the peak SGS eddy viscosity and dissipation are about 2.5 and 3 times the corresponding molecular values, respectively. The profiles also indicate the peak SGS dissipation is increased near the trailing edge to about six times the level of molecular dissipation. Figure 9d shows the ratio of the averaged backward and forward contribution to the model coefficient C (as defined in Ref. 16). The ratio is mostly constant over a significant part of the boundary layer. Figure 9e shows the percentage points, where $L_{ij}M_{ij}$ in Eq. (23) takes positive values, i.e., C being locally negative. It is clear from Fig. 9e that at the bump summit there is an increase in the number of points where C is negative, consistent with the time- and spanwise-averaged profile shown in Fig. 9a. As discussed in Sec. II.B, a clipping function was applied to remove the negative values of model coefficient after spanwise averaging at each time step. Figure 9f shows the ratio of the negative coefficient, which was clipped, and the actual model coefficient obtained in the calculation. As evident in Fig. 9f, the ratio is rather small with a maximum about 10% occurring at the summit, indicating that the (clipped) negative model coefficient is only a small fraction of the actual. Within the inner 20% of the boundary layer, the maximum in this ratio is less than 5%.

IV. Summary

The spatially developing three-dimensional TBL over a swept bump has been predicted using LES and RANS. The dynamic eddy viscosity model was applied in the LES, the v^2–f and the SA models were used in the RANS calculations. The three-dimensional TBL over the bump is an appropriate flow for application of techniques such as LES and RANS because it has well-defined upstream conditions and is a nontrivial test case, e.g., boundary-layer response is complex due to the repeated application/relaxation of streamwise pressure gradient, spanwise pressure gradient, and surface curvature. LES predictions of the mean flow, turbulence kinetic energy, and shear stresses are in good agreement with the experimental measurements of Webster et al.[2] and accurately capture the strong distortion of the flow over the bump surface as well as the rapid return to equilibrium over the downstream flat plate. Simple, equilibrium-based approximate boundary conditions were used in the LES, which correlate the instantaneous wall stress to LES velocity at the first layer of grid points. The mean wall stress, necessary to close the boundary conditions, was supplied a priori from experimental measurements or a separate RANS calculation. As also observed in the unswept bump, LES predictions of the outer flow were relatively insensitive to different prescriptions of the mean wall stress. The relatively accurate description of both the mean flow and turbulence quantities suggest that simple wall layer models may be reasonable for attached flows, though the problem of predicting the mean skin friction remains. It is also important to stress that separated flows will likely require more sophisticated approaches because existing wall layer models are not accurate.

Analysis of the strain rate indicates the present flow is representative of spatially developing three-dimensional TBLs produced over infinite geometries in the sense of possessing similar deformations, i.e., similar levels of distortion by the streamwise pressure gradient and mean-flow skewing. Thus, LES and dynamic models as well as the v^2–f and SA models should be expected to yield a similar level of agreement with measurements for other three-dimensional TBLs in this important category. In addition, the present results also support the notion discussed in Ref. 1 that isotropic eddy viscosity models applied to three-dimensional TBLs can yield acceptable predictions of the mean flow and skin friction, important for engineering applications. In particular, the agreement in the spanwise skin-friction coefficient with experimental data is extremely encouraging. Predictions of the mean velocity profiles using the v^2–f and SA models are in good agreement with the experimental measurements of Webster et al.[2] and do not show noticeable deterioration compared to the two-dimensional analog of the present flow due to the presence of mean-flow three dimensionality.

Acknowledgments

This work is supported by the U.S. Office of Naval Research (Grants N00014-94-1-0047 and N00014-94-1-1053, Program Officer L. Patrick Purtell). The authors gratefully acknowledge valuable discussions with P. A. Durbin, J. K. Eaton, T. S. Lund, D. R. Webster, and D. A. DeGraaff. Most of the simulations were performed on the Cray C90s and T90 at the U.S. Department of Defense High Performance Computing Major Shared Resource Centers (Corps of Engineers Waterways Experiment Station and Naval Oceanographic Office). Additional computing time was supplied by National Science Foundation Pittsburgh Supercomputing Center and Cornell Theory Center.

References

[1]Johnston, J. P., and Flack, K. A., "Review: Advances in Three-Dimensional Turbulent Boundary Layers with Emphasis on the Wall-Layer Regions," *Journal of Fluids Engineering*, Vol. 118, June 1996, pp. 219–236.

[2]Webster, D. B., DeGraaff, D. B., and Eaton, J. K., "Turbulence Characteristics of a Boundary Layer over a Swept Bump," *Journal of Fluid Mechanics*, Vol. 323, Sept. 1996, pp. 1–22.

[3]Bradshaw, P., and Pontikos, N. S., "Measurements in the Turbulent Boundary Layer on an Infinite Swept Wing," *Journal of Fluid Mechanics*, Vol. 159, Oct. 1985, pp. 105–130.

[4]Anderson, S. D., and Eaton, J. K., "Reynolds Stress Development in Pressure-Driven Three-Dimensional Turbulent Boundary Layers," *Journal of Fluid Mechanics*, Vol. 202, May 1989, pp. 263–294.

[5]Flack, A. K., and Johnston, J. P., "Near-Wall Investigation of Three-Dimensional Turbulent Boundary Layers," Dept. of Mechanical Engineering, Rept. MD-63, Stanford Univ., Stanford, CA, 1993.

[6]Schwarz, W. R., and Bradshaw, P., "Turbulence Structural Changes for a Three-Dimensional Turbulent Boundary Layer in a 30° Bend," *Journal of Fluid Mechanics*, Vol. 272, Aug. 1994, pp. 183–209.

[7]Simpson, R. L., and Olcmen, S. M., "An Experimental Study of a Three-Dimensional Pressure-Driven Turbulent Boundary Layer," *Journal of Fluid Mechanics*, Vol. 290, May 1995, pp. 225–262.

[8]Moin, P., Shih, T. H., Driver, D., and Mansour, N. N., "Direct Numerical Simulation of a Three-Dimensional Turbulent Boundary Layer," *Physics of Fluids A*, Vol. 2, No. 10, 1990, pp. 1846–1853.

[9]Sendstad, O., and Moin, P., "The Near Wall Mechanics of Three-Dimensional Turbulent Boundary Layers," Dept. of Mechanical Engineering, Rept. TF-57, Stanford Univ., Stanford, CA, 1992.

[10]Coleman, G. N., Kim, J., and Le, A. T., "A Numerical Study of Three-Dimensional Boundary Layers," *International Journal of Heat and Fluid Flow*, Vol. 17, No. 3, 1996, pp. 333–342.

[11]Coleman, G. N., Kim, J., and Spalart, P., "Direct Numerical Simulation of Three-Dimensional Swept-Wing Flows," *Bulletin of the American Physical Society*, Vol. 41, No. 9, 1996, p. 1826.

[12]Piomelli, U., Coleman, G., and Kim, J., "Effects of Mean Flow Three-Dimensionality on the Subgrid-Scale Stresses," *Bulletin of the American Physical Society*, Vol. 40, No.12, 1995, p. 1958.

[13]Bradshaw, P., Launder, B. E., and Lumley, J. L., "Collaborative Testing of Turbulence Models," *Journal of Fluids Engineering*, Vol. 118, June 1996, pp. 243–247.

[14]Germano, M., Piomelli, U., Moin, P., and Cabot, W. H., "A Dynamic Subgrid-Scale Eddy Viscosity Model," *Physics of Fluids A*, Vol. 3, No. 7, 1991, pp. 1760–1765.

[15]Moin, P., Squires, K. D., and Cabot, W., "A Dynamic Subgrid-Scale Model for Compressible Turbulence and Scalar Transport," *Physics of Fluids A*, Vol. 3, No. 11, 1991, pp. 2746–2757.

[16]Piomelli, U., "High Reynolds Number Calculations Using the Dynamic Subgrid-Scale Stress Model," *Physics of Fluids A*, Vol. 5, No. 6, 1993, pp. 1484–1490.

[17]Meneveau, C., Lund, T. S., and Cabot, W., "A Lagrangian Dynamic Subgrid-Scale Model of Turbulence," *Journal of Fluid Mechanics*, Vol. 319, July 1996, pp. 353–385.

[18]Ghosal, S., Lund, T. S., Moin, P., and Akselvoll, K., "A Dynamic Localization Model for Large Eddy Simulation of Turbulent Flows," *Journal of Fluid Mechanics*, Vol. 286, March 1995, pp. 229–255.

[19]Akselvoll, K., and Moin, P., "Large-Eddy Simulation of Turbulent Confined Coannular Jets," *Journal of Fluid Mechanics*, Vol. 315, May 1996, pp. 387–411.

[20]Lund, T. S., and Moin, P., "Large Eddy Simulation of a Boundary Layer of a Concave Wall Boundary Layer," *International Journal of Heat and Fluid Flow*, Vol. 17, No. 3, 1996, pp. 290–295.

[21]Piomelli, U., and Liu, J., "Large Eddy Simulation of Rotating Channel Flows Using a Localized Dynamic Model," *Physics of Fluids*, Vol. 7, No. 4, 1995, pp. 839–848.

[22]Wu, X., and Squires, K. D., "Numerical Investigation of the Turbulent Boundary Layer over a Bump," *Journal of Fluid Mechanics* (to be published).

[23]Wu, X., and Squires, K. D., "Large Eddy Simulation of an Equilibrium Three-Dimensional Turbulent Boundary Layers," *AIAA Journal*, Vol. 35, No.1, 1997, pp. 67–74.

[24]Durbin, P. A., "Separated Flow Computations with the K-ε-v^2 Model," *AIAA Journal*, Vol. 33, No. 4, 1995, pp. 659–664.

[25]Durbin, P. A., "A Reynolds Stress Model for Near-Wall Turbulence," *Journal of Fluid Mechanics*, Vol. 249, April 1993, pp. 465–498.

[26]Durbin, P. A., "On Modeling Three-Dimensional Turbulent Wall Layers," *Physics of Fluids A*, Vol. 5, No. 5, 1993, pp. 1231–1238.

[27]Wu, X., and Squires, K. D., "Prediction of the High Reynolds Number Flow over a Two-Dimensional Bump," *AIAA Journal* (to be published).

[28]Webster, D., DeGraaff, D., and Eaton, J. K., "Turbulence Characteristics of a Boundary Layer over a Two-Dimensional Bump," *Journal of Fluid Mechanics*, Vol. 320, Aug. 1996, pp. 53–69.

[29]Spalart, P. R., and Allmaras, S. R., "A One-Equation Turbulence Model for Aerodynamic Flows," *La Recherche Aerospatiale*, No. 1, 1994, pp. 5–21.

[30]Spalart, P. R., "Theoretical and Numerical Study of a Three-Dimensional Turbulent Boundary Layer," *Journal of Fluid Mechanics*, Vol. 205, Aug. 1989, pp. 319–340.

[31]Choi, H., Moin, P., and Kim, J., "Direct Numerical Simulation of Turbulent Flow over Riblets," *Journal of Fluid Mechanics*, Vol. 255, Oct. 1993, pp. 503–539.

[32]Ghosal, S., and Moin, P., "The Basic Equations for the Large Eddy Simulation of Turbulent Flows in Complex Geometry," *Journal of Computational Physics*, Vol. 118, No. 1, pp. 24–37.

[33]Lilly, D. K., "A Proposed Modification of the Germano Subgrid-Scale Closure Method," *Physics of Fluids A*, Vol. 4, No. 3, 1992, pp. 633–635.

[34]Jordan, S. A., and Ragab, S. A., "A Large-Eddy Simulation of the Near Wake of a Circular Cylinder," ASME FED Vol. 203, American Society of Mechanical Engineers, New York, 1994, pp. 1–9.

[35]Lund, T. S., Wu, X., and Squires, K. D., "On the Generation of Turbulent Inflow Conditions for Boundary Layer Simulations," *Annual Research Briefs*, Center for Turbulence Research, Stanford Univ., Stanford, CA, 1996, pp. 281–295.

[36]Lund, T. S., Wu, X., and Squires, K. D., "Generation of Turbulent Inflow Data for Spatially Developing Boundary Layer Simulations," *Journal of Computational Physics* (to be published).

[37]Schumann, U., "Subgrid Scale Model for Finite Difference Simulations of Turbulent Flows in Plane Channels and Annuli," *Journal of Computational Physics*, Vol. 18, No. 4, 1975, pp. 376–404.

[38]Piomelli, U., Ferziger, J., and Moin, P., "New Approximate Boundary Conditions for Large Eddy Simulations of Wall-Bounded Flow," *Physics of Fluids A*, Vol. 1, No. 5, 1989, pp. 1061–1068.

[39]Cabot, W., "Near-Wall Models in Large Eddy Simulations of Flow Behind a Backward-Facing Step," *Annual Research Briefs*, Center for Turbulence Research, Stanford Univ., Stanford, CA, Dec. 1996, pp. 199–210.

C. G. Speziale
Associate Editor